https://doi.org/10.5194/egusphere-2026-1156
Preprint. Discussion started: 23 March 2026

Subseasonal Predictability and Rossby Wave Dynamics of Blocking High during Transitional Seasons: Insights from Three Successive Events in May–June 2023

Zhixiang Li[1, 2], Jianhua Lu[1*], and Yimin Liu[2]

[1]School of Atmospheric Sciences, Sun Yat-sen University and Southern Marine Science and Engineering Guangdong Laboratory (Zhuhai), Zhuhai, People's Republic of China.

[2]Key Laboratory of Earth System Numerical Modeling and Application, Institute of Atmospheric Physics, Chinese Academy of Sciences, Beijing, People's Republic of China.

Submitted to *Weather and Climate Dynamics*

On Feb 28, 2026

[*]*Corresponding author*: Jianhua Lu (lvjianhua@mail.sysu.edu.cn)

https://doi.org/10.5194/egusphere-2026-1156
Preprint. Discussion started: 23 March 2026

Abstract

Extended-range prediction during the transitional seasons remains particularly challenging due to the volatile large-scale circulation background. This study investigates the dynamical linkages, Rossby wave characteristics, and subseasonal predictability of three successive atmospheric blocking events in May–June 2023, which contributed to severe Canadian wildfires, anomalous East Asian precipitation, and European heatwaves. The results indicate that the three blocking episodes are not independent but interconnected through downstream propagation of quasi-stationary Rossby wave energy. Spatiotemporal local diagnostics of phase speed, amplitude, and zonal wavenumber further reveal that all episodes are dominated by slowly propagating, large-amplitude planetary-scale Rossby waves in the troposphere, with zonal wavenumbers typically below the climatological zonal wavenumber. Day-to-day evolution shows abrupt transitions during blocking onset from an eastward-propagating synoptic-scale small-amplitude regime to a quasi-stationary or westward-propagating planetary-scale large-amplitude regime, with the reverse during blocking's decaying stage. ECMWF ensemble forecasts exhibit high predictability of 500 hPa geopotential height at 15–19-day lead times, with the best performance for the Ural blocking, where skillful members capture both the amplification of wave amplitude and spatial scale. In contrast, forecasts for the Canadian and European blocking show limited growth in wave parameters and associated geopotential height. For all episodes, skillful subseasonal predictions depend on capturing upstream quasi-stationary troughs over the North Pacific or North Atlantic, potentially influenced by exceptionally high sea surface temperatures in these basins during May–June 2023. These findings underscore that the growth in both amplitude and scale contributes to forecast errors in blocking circulation, while upstream wave precursors and external boundary forcing provide key sources of subseasonal predictability for persistent blocking circulation.

https://doi.org/10.5194/egusphere-2026-1156
Preprint. Discussion started: 23 March 2026

1 Introduction

The transitional seasons (spring and autumn) between winter and summer are typically short in duration and associated with abrupt change in general circulation over northern hemisphere (Yeh et al., 1959; Bordoni & Schneider, 2008; Yao et al., 2026). As such, the extended-range prediction (or subseasonal-to-seasonal, S2S prediction) during the transitional seasons is particularly difficult due to the volatile background of large-scale circulation (Breeden et al., 2022).

However, weather conditions during the transitional seasons can also be disastrous, as evidenced by extreme events that swept the globe during May–June 2023, such as the wildfires in Canada (Jain et al., 2024; Figs. 1a–b), floods in Italy (https://www.eumetsat.int/european-state-climate-2023; Fig. 1b), persistent precipitation in East Asia in late May (Gao & Gao, 2023; Fig. 1d), and heatwave in Northwest Europe in June (Berthou et al., 2024; Figs. 1e–f). Previous studies have shown that these extreme events were associated with regional persistent anticyclones or blocking in the troposphere (contours in Fig. 1). Therefore, understanding the mechanisms and predictability of such persistent circulation anomalies during transitional seasons are not only scientifically challenging, but also societally pivotal. To address this issue, we present a study on the dynamical mechanisms, interconnections, and subseasonal predictability of three successive blocking episodes in May–June 2023, from a global perspective.

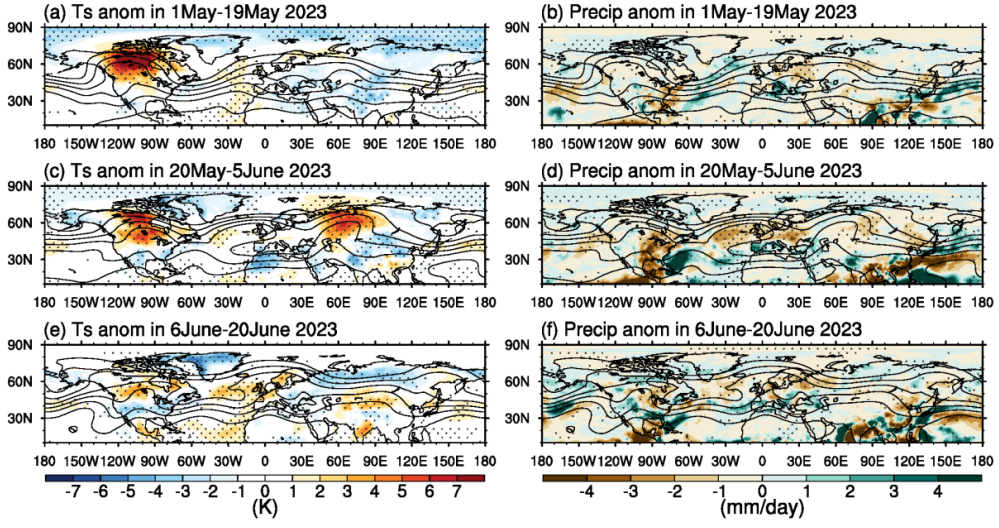

Figure 1. Anomalies of surface temperature (shading; left panels, a, c, e; units: K) and precipitation (shading; right panels, b, d, f; units: mm day^{-1}) during three successive episodes in 2023: 1–19 May (a, b), 20 May–5 June (c, d),

https://doi.org/10.5194/egusphere-2026-1156
Preprint. Discussion started: 23 March 2026

and 6–20 June (e, f). Stippling indicates regions where the anomalies of surface temperature or precipitation exceed 1 standard deviation (1σ). Solid black contours show the corresponding time-mean 500 hPa geopotential height (Z500).

Atmospheric blocking represents one of the most prominent modes of low-frequency variability in the extratropical troposphere. Several theories have been proposed for the dynamical mechanisms of blocking. For example, Pelly and Hoskins (2003) developed a wave-breaking theory, Luo et al. (2014) proposed a nonlinear multiscale interaction theory, and Nakamura and Huang (2018) introduced a local finite-amplitude wave activity framework. Comparative discussions of these theories can be found in Woollings et al. (2018) and Lupo (2021). From the perspective of wave propagation, blocking formation can be understood as the process by which a high-pressure ridge becomes quasi-stationary (Yeh et al., 1962). Using nonlinear multiscale interaction model, Luo et al. (2019) and Zhang et al. (2025) investigated the movement features of high-pressure ridges throughout the life cycle of blocking. They found that when blocking is strong and the meridional potential vorticity gradient is weak, the system exhibits pronounced westward movement and slower decay. Furthermore, owing to the planetary-scale nature of blocking circulation (Cheung et al., 2013; Luo et al., 2014), scale itself has been suggested as a potential impact factor of phase speed changes (Yeh et al., 1962; van Mourik et al., 2025).

Previous studies mainly defined the phase speed and scale of blocking based on the movement of the anticyclonic center and its zonal width (van Mourik et al., 2025; Zhang et al., 2025). Recently, however, a Hilbert transform-based method has been developed to quantitatively diagnose spatiotemporally local Rossby wave parameters (Fragkoulidis & Wirth, 2020; Li et al., 2025). This approach allows direct calculation of local phase speed, amplitude, and wavenumber during the life cycle of blocking. In this paper, we shall diagnose both the time-mean and day-to-day evolution of Rossby wave parameters to uncover the characteristics of Rossby waves and their links to surface extreme weathers during the blocking episodes of May–June 2023. The diagnosed phase speed and wavenumber can also be compared with the stationary wavenumber that have recently been widely used in the studies of quasi-stationary waves (Fei & White, 2025; White & Mareshet Admasu, 2025).

The subseasonal predictability of blocking remains a major challenge (Kautz et al., 2022). It is therefore of interest to evaluate the subseasonal forecast of the ECMWF S2S model for the

https://doi.org/10.5194/egusphere-2026-1156
Preprint. Discussion started: 23 March 2026

blocking anticyclones during the transitional season of 2023, and to investigate how subseasonal forecast errors in blocking anticyclones are linked to errors in Rossby wave parameters. In short, we aim in this study to investigate the dynamical linkages, Rossby wave parameters, and subseasonal predictability of three successive atmospheric blocking episodes in May–June 2023. The remainder of this study is organized as follows. Section 2 describes the data and methods. Section 3 presents the results. Section 4 provides a summary and discussion.

2 Data and Methods

2.1 Data

In this study, we use zonal wind (u), meridional wind (v) and geopotential height (Z) from ERA5 reanalysis data (Hersbach et al., 2020) for the period from 1979 to 2023 with a temporal resolution of 6–hourly (daily at 0000, 0600, 1200 and 1800 UTC) and a horizontal resolution of 2.5°×2.5°. The Global Precipitation Climatology Project (GPCP) daily precipitation with 1°×1° spatial resolution from 1997 to 2023 (Huffman et al., 2001) are used to investigate the large-scale precipitation anomalies. The monthly mean sea surface temperature (SST) from 1997 to 2023 with a horizontal resolution of 2°×2° come from the Extended Reconstructed Sea Surface Temperature, version 5 (ERSSTv5) dataset (Huang et al., 2017). Additionally, the daily Z with a horizontal resolution of 1.5°×1.5° from the 50-member ensemble of the ECMWF real-time S2S prediction system are utilized. The Z of S2S is interpolated to the same resolution as ERA5 to facilitate the comparison.

2.2 Local Wave Parameters Diagnostic Method

The local wave parameters diagnostic method is conducted by applying the Hilbert transform to 6-hourly geopotential height (Fragkoulidis & Wirth, 2020; Li et al., 2025). The convolution-based Hilbert transform of wave signal s at each longitude n is given by,

$$\hat{s}(n) = \sum_{m=-\infty}^{m=\infty} s(n-m)h(m) \approx \sum_{m=-M}^{m=M} s(n-m)h(m) \quad (1)$$

$$\text{where} \quad h(m) = \begin{cases} \frac{2}{m\pi}\sin^2\left(\frac{m\pi}{2}\right), & m \neq 0 \\ 0, & m = 0 \end{cases} \quad m = -M, \dots, 0, \dots, M \quad (2)$$

n is the grid-point index along the zonal circle, and m represents the number of grids shifted in the convolution calculation, with the maximum shift M is set to 144, corresponding to the 2.5° ×

https://doi.org/10.5194/egusphere-2026-1156
Preprint. Discussion started: 23 March 2026

2.5° horizontal resolution of the dataset. Second, construct the complex signal $S = s + \mathrm{i}\hat{s}$, and express it in the polar form $S = E\mathrm{e}^{\mathrm{i}\phi}$, where E is the local envelope or amplitude calculated from the polar radius of S, i.e.,

$$E=\sqrt{s^2+\hat{s}^2} \tag{3}$$

and ϕ is the local phase calculated from the polar angle of S,

$$\phi = \tan^{-1}\left(\frac{\hat{s}}{s}\right) \tag{4}$$

By introducing the plane wave hypothesis, the local angular frequency ω and local zonal wavenumber k can be obtained from

$$\begin{cases} \omega = -\dfrac{\partial\phi}{\partial t} \\ k = \dfrac{\partial\phi}{\partial x} = \dfrac{1}{a\cos\varphi}\dfrac{\partial\phi}{\partial\lambda} \end{cases} \tag{5}$$

where notations are standard. Finally, the local wave period T is defined as

$$T = \frac{2\pi}{|\omega|} \tag{6}$$

while the local zonal phase speed can be obtained from

$$C_{px} = \frac{\omega}{k} \tag{7}$$

The reader is referred to Li et al. (2025) for full technical details. The method of Li et al. (2025) identifies physically meaningless results (e.g., negative zonal wavenumbers and neighboring grids) as missing values, thus allowing its application to any input wave signal (e.g., zonal wavenumbers 1–15 Z500 in this study) without the need for specific threshold for amplitude as in Fragkoulidis & Wirth (2020).

2.3 The Detection of Atmospheric Blocking

The Tibaldi-Molteni blocking index (Tibaldi and Molteni, 1990) is used to identify the timing and locations of large-scale blocking events during May–June 2023. The index is defined based on the reversal of the meridional gradient of Z500,

$$GHGN = [Z500(\phi_N) - Z500(\phi_0)]/(\phi_N - \phi_0) \tag{8}$$

$$GHGS = [Z500(\phi_0) - Z500(\phi_S)]/(\phi_0 - \phi_S) \tag{9}$$

where $\phi_N = 80°N + \Delta$, $\phi_0 = 60°N + \Delta$, $\phi_S = 40°N + \Delta$, and $\Delta = -5°, 0°, 5°$. Large-scale blocking events are defined as those satisfying $GHGN < -10\ gpm/degree$ and $GHGS > 0$, with the condition persisting over at least 15 degrees of longitude and for 4 consecutive days.

https://doi.org/10.5194/egusphere-2026-1156
Preprint. Discussion started: 23 March 2026

2.4 Wave Activity Flux and Stationary Wavenumber

Horizontal propagation of quasi-stationary waves is diagnosed using the wave activity flux of Takaya & Nakamura (2001),

$$WAF = \frac{p}{2|U|}\begin{Bmatrix}\bar{u}\left(\psi_x'^{\,2} - \psi'\psi_{xx}'\right) + \bar{v}\left(\psi_x'\psi_y' - \psi'\psi_{xy}'\right) \\ \bar{u}\left(\psi_x'\psi_y' - \psi'\psi_{xy}'\right) + \bar{v}\left(\psi_y'^{\,2} - \psi'\psi_{yy}'\right)\end{Bmatrix} \quad (10)$$

The overbar and primes represent the climatological mean and the anomalies during each episode, respectively. p and ψ denotes the pressure normalized by 1000 hPa and geostrophic stream function, respectively. $U = (u, v)$. The anomalies in this study are calculated as the temporal mean in each episode, with the corresponding climatological mean and linear trend removed. This approach isolates the quasi-stationary waves, as the averaging filters out transient disturbances. The statistical significance is assessed based on the two-tailed Student's *t*-test.

Following Hoskins and Ambrizzi (1993) and Lubis et al. (2024), the stationary wavenumber K_s is defined as

$$K_s = a\cos\varphi\left(\frac{\beta^*}{\bar{U}}\right)^{1/2} \quad (11)$$

where $\bar{U}$ is the zonal and time mean of 500 hPa zonal wind between 16 April and 30 June 2023, β^* is the meridional gradient of absolute vorticity in a spherical coordinate system.

3 Results

3.1 Evolution of Blocking Episodes and Waves Activity Flux

Based on the timing of the Canadian blocking, the Ural blocking (quasi-stationary ridge), and the European blocking, along with the corresponding occurrences of the Canadian wildfires, East Asian precipitation anomalies, and the European heatwave, we divided May–June 2023 into three consecutive episodes (Fig. 2).

During episode 1 (1–19 May, 2023), a strong quasi-stationary ridge persists over the Canadian region, accompanied by two large-scale blocking events (dotted regions in Fig. 2a). A quasi-stationary Rossby wave train is evident from the North Pacific to the Mediterranean region, while Canada lies under the control of a strong ridge (Fig. 3a). Wave activity flux further shows that quasi-stationary wave energy disperses downstream from the North Pacific toward the Mediterranean, with Canada located in the convergence zone of upstream wave activity flux, favoring the maintenance of the high-pressure ridge (Fig. 3a).

https://doi.org/10.5194/egusphere-2026-1156
Preprint. Discussion started: 23 March 2026

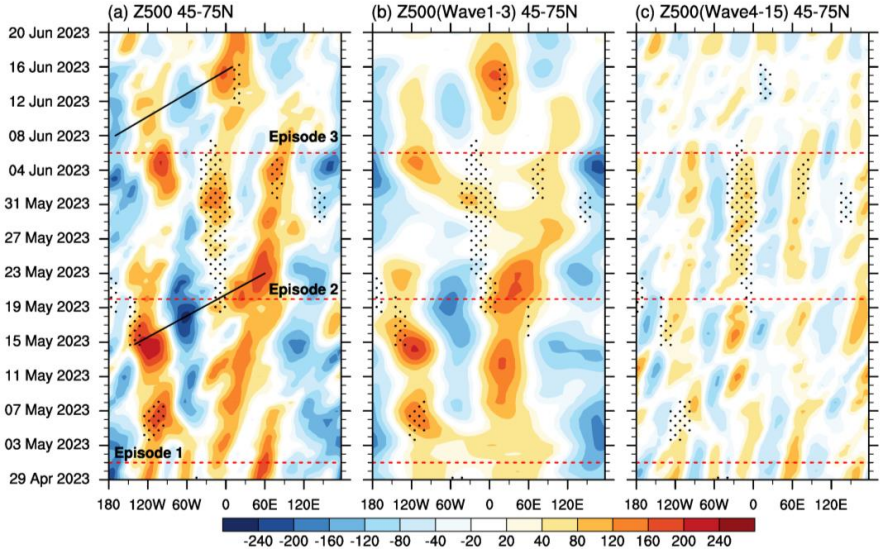

Figure 2. Hovmöller diagrams of zonal-mean-removed (a), 1–3-wave (b) and 4–15-wave (c) Z500 (units: gpm) averaged over 45° and 75°N during three successive episodes in May–June 2023. Black lines in (a) show the downstream development of Rossby waves. Black dots mark the locations of identified large-scale blocking events.

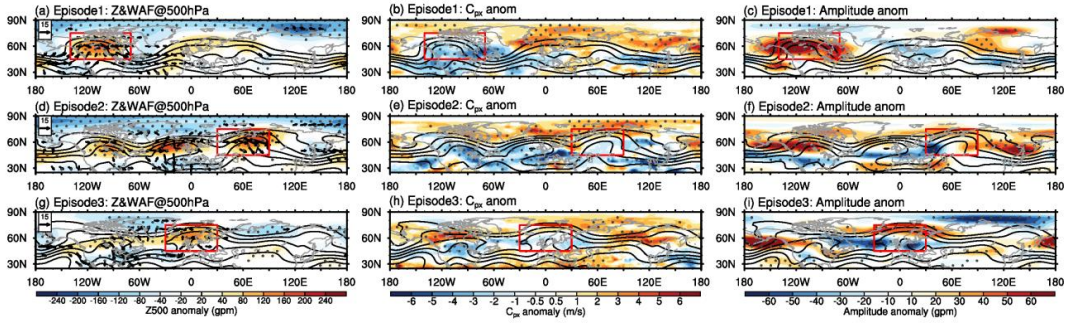

Figure 3. Anomalies of Z500 (shading; left panels, a, d, g; units: gpm), zonal phase speed (shading; middle panels, b, e, h; units: m s^{-1}), and wave amplitude (shading; right panels, c, f, i; units: gpm) at 500 hPa during (a–c) episode 1, (d–f) episode 2, and (g–i) episode 3. Stippling indicates anomalies exceeding 1σ. Solid black contours show the corresponding time-mean Z500. Vectors in the left panels represent the wave activity flux at 500 hPa (units: m^2 s^{-2}).

In episode 2 (20 May–5 June, 2023), the strong Canadian ridge weakens, while the large-scale blocking events establish over Europe and the Ural Mountains (Fig. 2a). Correspondingly, the energy propagation of quasi-stationary wave weakens in the upstream of Canada (i.e., over the northeastern Pacific), while downstream propagation toward Europe and the Ural Mountains strengthens, thereby favoring the formation and maintenance of the European and Ural ridges.

https://doi.org/10.5194/egusphere-2026-1156
Preprint. Discussion started: 23 March 2026

The downstream development is also evident in the Hovmöller diagram in Fig. 2a after the Canadian anticyclone begins to decay and then collapses (black line between 15–23 May).

During episode 3 (6–20 June, 2023), both the Canadian and Ural ridges weakened substantially, while a new large-scale blocking event develops over Europe between 11–16 June (Fig. 2a). From the perspective of wave activity flux, the energy propagation originating from North America splits into two branches, one disperses southeastward toward the northwestern Atlantic and the other propagates northeastward via Greenland toward Europe. Europe is situated in the convergence zone of both the northern and southern branches of wave activity flux, which favors the formation of the European blocking. The downstream development over the North America-to-Europe sector is also apparent from the Hovmöller diagram between 8–16 June (Fig. 2a).

3.2 Results from the Local Wave Parameters

Local wave parameter diagnostic method is utilized to further uncover the C_{px}, amplitude and zonal wavenumber of Rossby waves during each episode. In this section, we analyze the temporal mean and temporal evolutions of these wave parameters for each episode, with particular focus on their relationships to the blocking circulation.

3.2.1 Episode 1

In episode 1, from the northeastern Pacific to the eastern North Atlantic, markedly low phase speeds (Fig. 3b) and strongly enhanced wave amplitudes (Fig. 3c) are observed. Clearly, the slowly moving, large-amplitude ridge is the dominant circulation factor responsible for the Canadian wildfires.

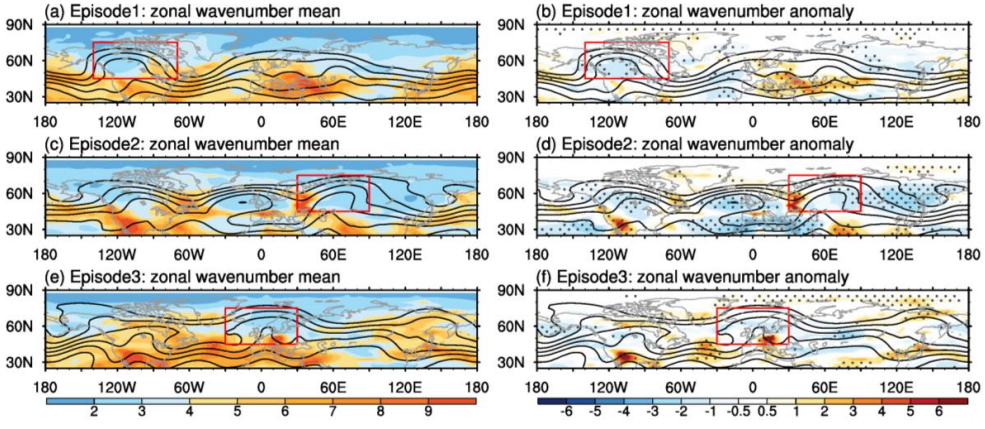

https://doi.org/10.5194/egusphere-2026-1156
Preprint. Discussion started: 23 March 2026

Figure 4. Time-mean zonal wavenumber (shading; left panels: a, c, e) and its anomalies (shading; right panels: b, d, f) at 500 hPa averaged during (a, b) episode 1, (c, d) episode 2, and (e, f) episode 3. Stippling in the right panels indicates anomalies exceeding 1σ. Black solid contours show the corresponding time-mean Z500.

Local zonal wavenumber diagnostics further indicate that the Canadian blocking is dominated by wavenumbers 2–4 (Fig. 4a), which is lower than its climatological mean by one wavenumber or higher (Fig. 4b). The dominance of planetary-scale waves is also evident in the Hovmöller diagrams, as seen by comparing Fig. 2b and Fig. 2c. Due to the scale effects, the anomalously small wavenumber over Canada contributes to the unusually slow phase speed of the ridge (as shown in Fig. 3b) and enables the long-wave ridge to maintain a quasi-stationary state. Interestingly, upstream, downstream, and on the southern side of the Canadian blocking, the Rossby waves are instead dominated by slowly moving synoptic-scale waves (Fig. 3b and Fig. 4a), suggesting possible interactions between planetary-scale blocking and surrounding synoptic-scale waves.

The relationships between the temporal evolutions of wave parameters during the onset, maintenance, and collapse of the blocking are further shown in Figure 5. Corresponding to the two large-scale blocking events in episode 1, Z500 and wave amplitude exhibit two distinct peaks (>1σ; deep pink in Fig. 5a), while C_{px} and zonal wavenumber show two pronounced minima (<-1σ; deep blue in Fig. 5a). During the onset of the first blocking event (May 1–5), as Z500 rapidly strengthens (Fig. 5a), C_{px} decreases sharply from more than 3 m s^{-1} to negative values (Fig. 5d), wave amplitude rapidly increases from negative anomalies to >1σ (Fig. 5g), and the dominant scale abruptly shifted from synoptic-scale (local zonal wavenumber >6) to planetary-scale (around zonal wavenumber 3, less than $K_s \approx 4$) (Fig. 5j). In the subsequent decay stage of the first blocking anticyclones (7–10 May), although amplitude decreases, a planetary-scale ridge with near-zero phase speed still persists over Canada, and the local zonal wavenumber approaching the K_s.

A similar rapid evolution recurs during the second onset stage (12–15 May). Following the collapse of the second blocking event, Rossby waves over Canada change from westward-propagating large-amplitude planetary-scale waves to eastward-propagating small-amplitude synoptic-scale waves, with these rapid changes occurred within a few days. These results indicate that the onset and decay of blocking are both accompanied by abrupt transitions in wave parameters.

https://doi.org/10.5194/egusphere-2026-1156
Preprint. Discussion started: 23 March 2026

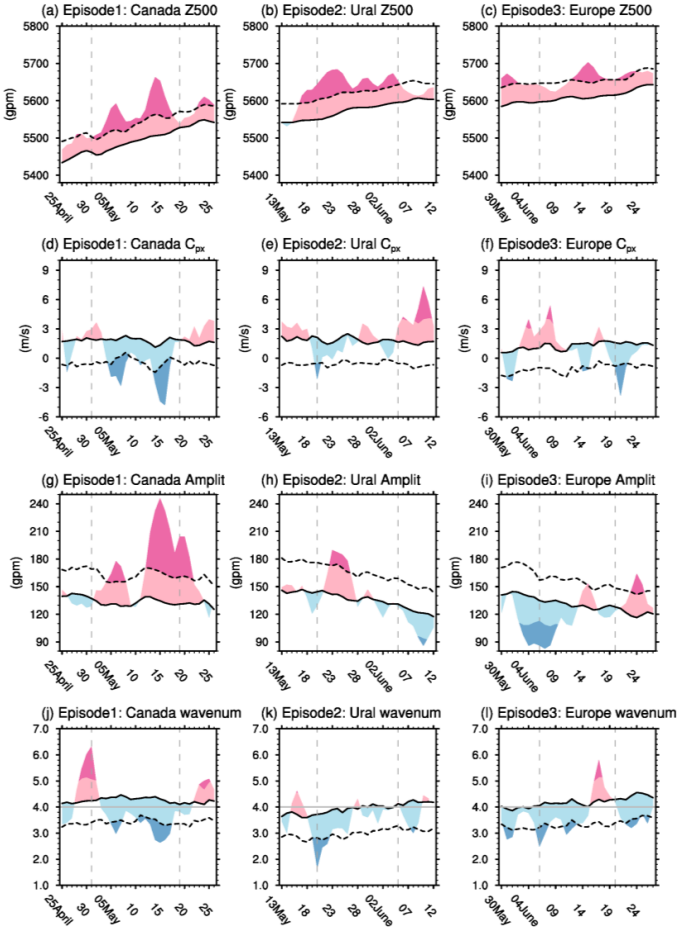

Figure 5. Daily evolution of area-averaged Z500 (a–c; units: gpm), zonal phase speed (d–f; units: m s^{-1}), wave amplitude (g–i; units: gpm), and zonal wavenumber (j–l) at 500 hPa during different blocking episodes. The three panels (from left to right) correspond to the averaged over the Canada (a, d, g, j), the Ural Mountains (b, e, h, k), and Europe (c, f, i, l), respectively. The averaging regions are indicated by the red boxes in Figs. 3 and 4. In each panel, pink and dark pink shading indicate values exceeding the daily climatology (black solid line) and +1σ (black dashed line in a–c and g–i), respectively. Blue and dark blue shading indicate values below the daily climatology (black solid line) and –1σ (black dashed line in d–f and j–l), respectively. Gray solid lines in (j–l) denote the stationary wavenumber K_s. Gray vertical dashed lines mark the start and end dates of each episode.

3.2.2 Episode 2

In this episode, wave amplitude over Canada remains anomalously strong (Fig. 3f), likely contributing to the continued severity of wildfires in late May. Over Eurasia, enhanced wave amplitude extends from the ridge over Ural Mountains to trough over the Okhotsk Sea (Fig. 3f).

https://doi.org/10.5194/egusphere-2026-1156
Preprint. Discussion started: 23 March 2026

Corresponding to the quasi-stationary waves over Canada, Europe and Eurasia, anomalously low C_{px} prevail across the entire midlatitudes (Fig. 3e). The European and Ural blocking in episode 2 are likewise dominated by wavenumbers 2–4 (Fig. 4c), with the anomalously low wavenumbers across the midlatitudes (Fig. 4d) corresponding to the anomalously slow phase speeds. Overall, the slowly moving planetary-scale large-amplitude East Asian trough–ridge pattern facilitates persistent southward transport of cold air, contributing to positive precipitation anomalies in East Asia.

Although the large-scale blocking event forms between 31 May and 5 June, the strong ridge indeed persists from 17 May to 5 June (Fig. 2a and Fig. 5b). During the early formation stage of the ridge (17–23 May), a rapid decrease in phase speed and zonal wavenumber occurs (Fig. 5e and Fig. 5k), accompanied by a rapid increase in wave amplitude (Fig. 5h), as in episode 1. However, unlike the westward propagation seen in episode 1, the Ural quasi-stationary ridge exhibits C_{px} oscillating around 1.5 m s^{-1} during the maintenance stage (Fig. 5e), suggesting weak eastward propagation characteristics (as also shown in Fig. 2a), In this stage, zonal wavenumbers are close to or slightly below the K_s (Fig. 5k). After 5 June, wave amplitude decreases while C_{px} increases sharply, indicating rapid weakening and downstream movement of the circulation system after the collapse of the Ural blocking event.

3.2.3 Episode 3

In episode 3, anomalously low phase speeds but relatively modest wave amplitudes characterize the circulation pattern extending from the mid-latitude North Atlantic to Europe (Fig. 3h and 3i). Positive wave amplitude anomalies mainly appear north of the European block, i.e., from southern Greenland to northern Europe (Fig. 3i). The European blocking in the third episode is also dominated by zonal wavenumbers 2–4 (Fig. 4e), consistent with negative phase speed anomalies there (Fig. 3h). However, compared with Episodes 1 and 2, both the intensity and spatial extent of the large-amplitude anomaly over Canada decrease markedly in episode 3 (Fig. 3i). Moreover, phase speed anomalies north of 60°N over Canada turn positive (Fig. 3h), and the dominant zonal wavenumber over Canada shifts to 4–6 (Fig. 4e), indicating a transition from a large-amplitude quasi-stationary planetary-scale ridge to eastward-propagating synoptic-scale waves.

During the onset and maintenance of the European blocking (11–15 June), C_{px} decreases rapidly while wave amplitude increases rapidly. When Z500 and amplitude reach their maxima,

https://doi.org/10.5194/egusphere-2026-1156
Preprint. Discussion started: 23 March 2026

C_{px} reaches its minimum and becomes westward. In this period the zonal wavenumber remains between 3 and 4, slightly below the K_s. After the collapse of the blocking (16–20 June), Z500 and amplitude decrease sharply, and the Rossby waves transitions from westward-propagating planetary-scale waves to eastward-propagating synoptic-scale waves.

3.3 The dynamic source of predictability in ECMWF ensemble forecasts

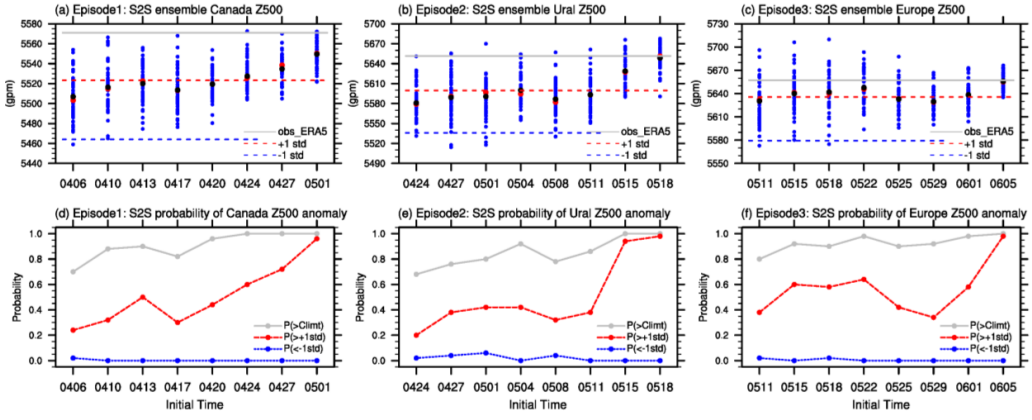

Figure 6. (a–c) ECMWF S2S forecasted time- and spatially averaged Z500 for episode 1 (a), episode 2 (b), and episode 3 (c). The three panels (from left to right) correspond to averages over the Canada (a), the Ural Mountains (b), and Europe (c), respectively. Each blue dot represents one of the 50 ensemble members. Black (red) dots denote the ensemble mean (median). In each episode, the solid gray line shows the observed time- and spatially averaged Z500 in 2023 from ERA5, while the red and blue dashed lines indicate the observed +1σ and –1σ bounds based on ERA5 from 1979–2023, respectively. (d–f) Probabilities of forecasted time-mean Z500 exceeding the climatological mean (gray line), exceeding +1σ (red line), and falling below –1σ (blue line) as a function of initialization date for episode 1 (d), episode 2 (e), and episode 3 (f). The abscissa represents forecast initialized dates with twice weekly.

It is interesting to check the capability of ensemble forecasts by ECMWF model in forecasting the blocking circulation in these three episodes. Figures 6a–c shows the forecasted temporal mean Z500 during each episode based on the 50 members. The subseasonal forecast results for these three episodes exhibit notable similar features. First, for each episode we note that very few members (usually less than 2) predicting a negative anomaly (less than -1σ) with almost all of initialization dates (blue lines in Figs. 6d–f). Remarkably, for the forecasts initialized 15–19 days ahead of each episode, i.e. initialized at 13 April for episode 1 (Figure 6d), initialized at 1 May and 4 May for episode 2 (Figure 6e), and initialized from 15 May to 22 May for episode 3 (Figure 6f), there are usually 40%–65% of the total 50 members (20–32 members)

https://doi.org/10.5194/egusphere-2026-1156
Preprint. Discussion started: 23 March 2026

predicting a positive anomaly (larger than +1σ, red lines in Figs. 6d–f), and more than 80% of the total member predicting a temporal mean Z500 above the climate mean (gray lines in Figs. 6d–f). The predictability drops for the forecasts made during the following week, but the number of correct-forecast members increases markedly and becomes dominant for initializations made 2–5 days ahead of each episode. In the following sections we try to understand the sources of predictability two weeks in advance for these three episodes, and examine how forecast errors relate to errors in wave parameters.

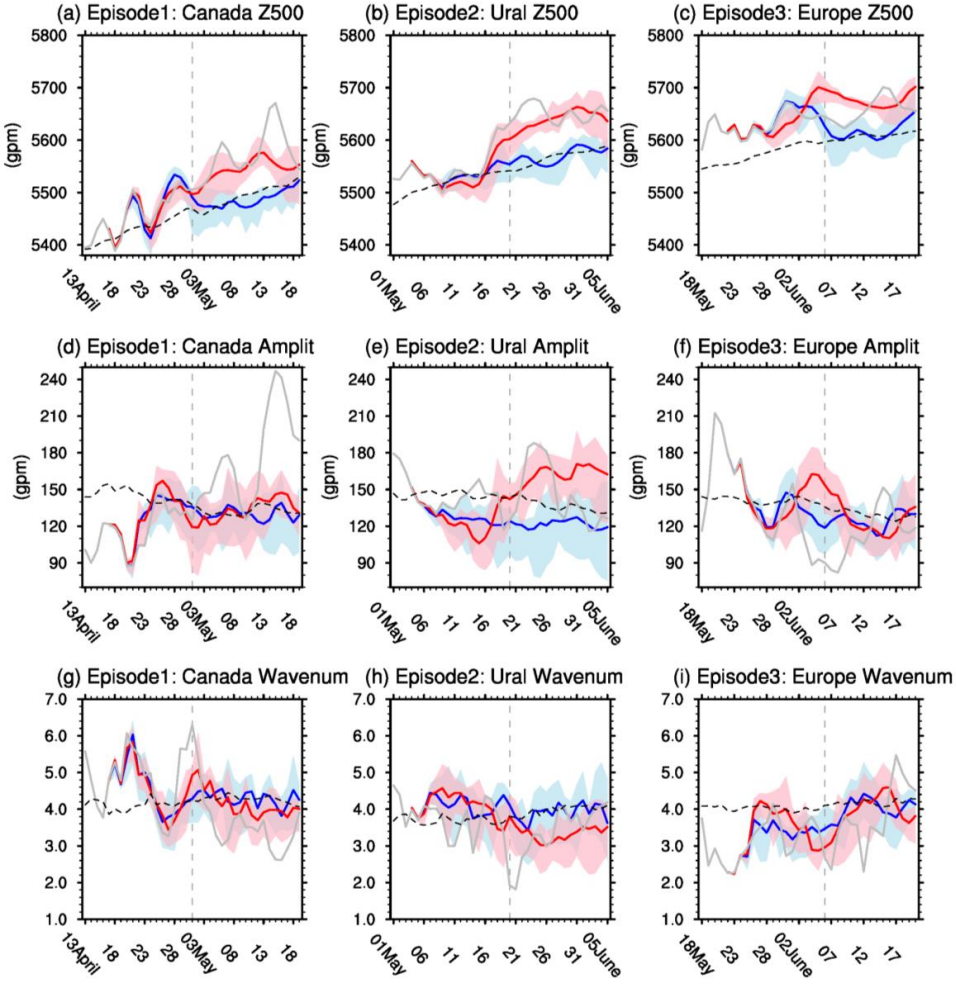

Figure 7. Daily evolution of ECMWF S2S forecasted spatially averaged Z500 (a–c; units: gpm), wave amplitude (d–f; units: gpm), and zonal wavenumber (g–i) at 500 hPa during different episodes. The three panels (from left to right) correspond to averages over the Canada (initialized at 17 April; a, d, g), the Ural Mountains (initialized at 4 May; b, e, h), and Europe (initialized at 22 May; c, f, i), respectively. In each panel, red and blue solid lines

https://doi.org/10.5194/egusphere-2026-1156
Preprint. Discussion started: 23 March 2026

represent the ensemble means of the good-forecast ensemble members and bad-forecast ensemble members, respectively, while the pink and light blue shading indicate the 20%–80% spread of the good and bad members, respectively. The gray solid line and the black dashed line denotes the observed daily evolution in 2023 and observed daily climatology based on ERA5, respectively. Vertical gray dashed lines mark the onset day of each episode.

Figure 7 compares the day-to-day evolutions in Z500, wave amplitude, and zonal wavenumber between the good-forecast and bad-forecast ensembles' forecasts initialized approximately two weeks ahead for each episode. In each episode, the good members and bad members are defined as the 10 members with the strongest and weakest time- and spatially averaged Z500 over the blocking region, respectively. The initialization dates are 17 April (14 days lead) for episode 1, 4 May (16 days lead) for episode 2, and 22 May (15 days lead) for episode 3. Among the three episodes, episode 2 (the quasi-stationary ridge over the Ural Mountains) shows the best forecast skill. The good ensembles successfully capture both the intensity and duration of the Z500 anomaly seen in ERA5, whereas the bad ensembles fail to predict the amplification of Z500 after 18 May (Fig. 7b). The good ensembles also forecast the amplification of wave amplitude and spatial scale after 18 May (Figs. 7e and 7h). For episode 1 (the blocking over Canada), even the good ensembles predict a Z500 intensity of only about half the observed value (Fig. 7a), with correspondingly limited growth in wave amplitude and scale (Figs. 7d and 7g). In episode 3 (the blocking over Europe), although the good ensembles predict the prolonged positive Z500 anomaly after 6 May, the forecasted peak of Z500 occurs noticeably earlier than in ERA5 (Fig. 7c). Similarly, forecasts of wave parameters in episode 3 show weaker amplification, such that the good and bad ensembles exhibit no clear differences in either amplitude or scale after 8 June. Overall, forecasts of wave amplitude and scale perform more poorly than those of Z500, particularly in episodes 1 and 3.

https://doi.org/10.5194/egusphere-2026-1156
Preprint. Discussion started: 23 March 2026

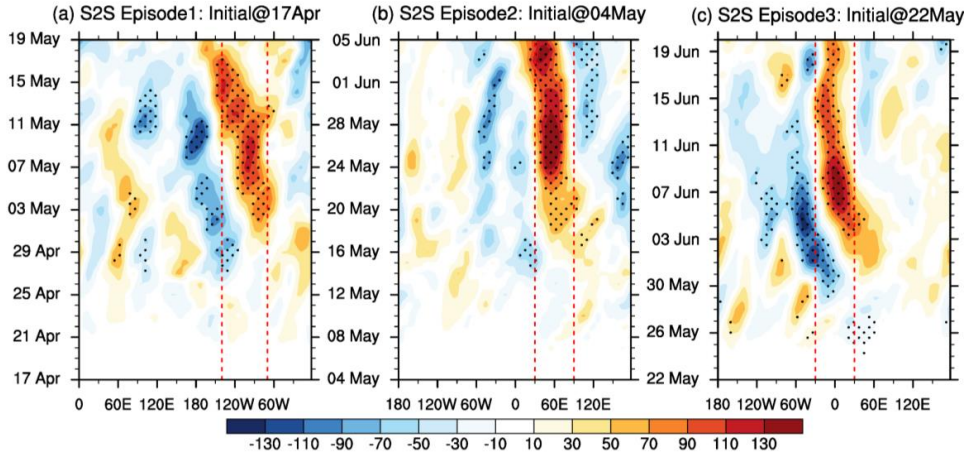

Figure 8. Hovmöller diagrams of ensemble-mean Z500 differences (shading; units: gpm) between good- and bad-forecast members for (from left to right) the Canadian blocking (initialized at 17 April; a), Ural blocking (initialized at 4 May; b), and European blocking (initialized at 22 May; c). Stippling denotes the differences are statistically significant above the 95% confidence level. The region between the red dashed lines in (a)–(c) indicates the Canada, the Ural Mountains, and Europe, respectively.

To further elucidate the sources of subseasonal predictability for these three episodes, we examine the ensemble-mean differences in Z500 between the good and bad ensembles, as shown in the Hovmöller diagrams in Figure 8. The three episodes display similar pattern, with pronounced differences emerging after approximately 10 days after initialization and showing a clear connection to upstream quasi-stationary troughs. For episode 1, the good ensembles not only predict the quasi-stationary ridge over Canada but also capture the quasi-stationary trough over the North Pacific (Fig. 8a). For episodes 2 and 3, in addition to the quasi-stationary ridges over the Ural region and Europe, respectively, the good ensembles consistently predict the presence of an upstream trough over the North Atlantic (60°W–0°E) (Figs. 8b–c). Across all three episodes, the trough–ridge relationship exhibits a clear downstream development, indicating that accurate prediction of the upstream quasi-stationary trough plays a crucial role.

4 Summary and discussion

This study investigates the subseasonal dynamical processes and predictability associated with three consecutive large-scale blocking episodes over Canada and Eurasia during May–June 2023, using ERA5 reanalysis data, ECMWF S2S ensemble forecasts, and local wave parameter diagnostics. The main conclusions are as follows:

https://doi.org/10.5194/egusphere-2026-1156
Preprint. Discussion started: 23 March 2026

1. The three blocking events are dynamically linked through the energy propagation of quasi-stationary Rossby waves. During episode 1 (1–19 May), wave activity flux originating from the North Pacific favors the maintenance of the Canadian blocking. Following the collapse of the Canadian blocking, the wave energy propagates downstream toward Europe and the Ural region, promoting the establishment and persistence of the ridges in episode 2 (20 May–5 June). In episode 3 (6–20 June), the quasi-stationary wave energy propagation over the North America–North Atlantic sector splits into branches that converge over Europe, thereby favoring the formation and maintenance of the European blocking.

2. Based on the local wave parameter diagnostics, all three blocking episodes are dominated by slowly propagating (anomalously low phase speed), large-amplitude planetary-scale Rossby waves with zonal wavenumbers typically in the range 2–4, which are lower than their climatological zonal wavenumber and often fall below the stationary wavenumber K_s. These anomalous tropospheric Rossby wave characteristics are closely linked to the development and persistence of surface extreme weather. In particular, the slowly propagating large-amplitude ridge over Canada during episodes 1 and 2 creates prolonged dry and warm conditions conducive to intense Canadian wildfires, while the slowly moving planetary-scale large-amplitude trough–ridge pattern over Eurasia in episode 2 supports persistent cold-air outbreaks and precipitation anomalies in East Asia.

3. During blocking onset, the wave parameters undergo a rapid transition from eastward-propagating, small-amplitude synoptic-scale waves to quasi-stationary or westward-propagating, large-amplitude planetary-scale waves, with the reverse transition occurring during decay. During the onset and maintenance stages of blocking, the zonal wavenumber tends to be smaller than the K_s. In particular, the phase speed becomes negative when the amplitude and scale reach their maximum, facilitating the retrograde behavior of the blocking circulation. These abrupt shifts in phase speed, amplitude, and wavenumber typically occur over just a few days, highlighting the pronounced abrupt intraseasonal transitions in Rossby wave regime.

4. For all three blocking episodes, the ECMWF S2S ensemble-mean forecasts exhibit high accuracy at short lead times of 2–5 days. However, the ensemble forecasts demonstrate meaningful subseasonal predictability when initialized 15–19 days ahead. Among the episodes, episode 2 displays the highest forecast skill, with good ensembles successfully reproducing both the intensity and duration of the Ural ridge as well as the associated amplification in wave

https://doi.org/10.5194/egusphere-2026-1156
Preprint. Discussion started: 23 March 2026

amplitude and scale. In contrast, the bad ensembles fail to capture the growth in amplitude and scale. Overall, forecasts of wave amplitude and scale perform markedly worse than those of Z500, particularly in episodes 1 and 3. Ensemble-mean differences between good and bad ensembles reveal that skillful subseasonal forecasts are closely linked to representation of upstream quasi-stationary troughs (over the North Pacific in episode 1 and over the North Atlantic in episodes 2 and 3), underscoring the critical role of upstream wave precursors in determining the subseasonal predictability of blocking circulations.

The transition from small-amplitude transient synoptic-scale waves to large-amplitude quasi-stationary planetary-scale waves during blocking onset aligns with previous studies (Luo et al., 2014; Woollings et al., 2018). As suggested in Luo et al. (2019) and Zhang et al. (2025), the present study also shows that when the amplitude of blocking reaches its maximum, the blocking system generally tends to propagate westward. What distinguishes this work from prior researches is the application of the Hilbert transform to quantitatively diagnose the local phase speed, amplitude and wavenumber throughout the life cycle of blocking, thereby enabling a detailed analysis of the evolution relations among them. Furthermore, we find that the evolution of wavenumber is also important for blocking movement (Yeh et al., 1962; van Mourik et al., 2025). In the future, this method could be extended to statistical analyses of the links between blocking wave parameters and surface extreme weathers, as well as to quantitative evaluations of model performance.

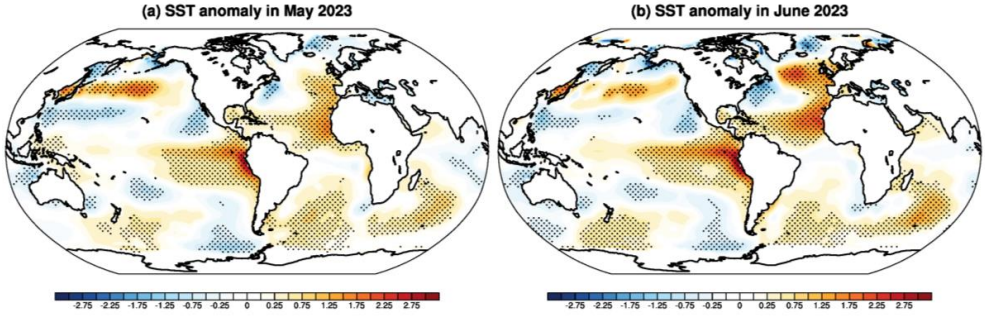

Figure 9. SST anomalies in May (a) and June (b) 2023 (units: ℃). Stippling indicates anomalies exceeding 1σ.

The subseaseaonal upstream wave precursors over the North Pacific and North Atlantic appear to be linked to the exceptionally high sea surface temperatures in these two basins during May–June 2023 (Fig. 9). In fact, recent studies on the Canadian wildfires in May–September 2023 have suggested that the anomalously warm North Pacific SST excited a quasi-stationary

https://doi.org/10.5194/egusphere-2026-1156
Preprint. Discussion started: 23 March 2026

wave train propagating toward North America (Wu et al., 2025). Our study, from a subseasonal perspective, highlights the importance of midlatitude SST anomalies for the evolution of circulation patterns and forecast skill during the transitional season. In addition, we also note that the predictability of ensemble forecasts may oscillate between leading-time of 15 and 5 days (Figs. 6d–f), which highlights the importance of supplementary diagnostic methods in understanding this phenomenon and in sorting out the better ensemble members (Mu & Duan, 2025).

Acknowledgments

Jianhua LU and Zhixiang LI appreciate the support from the National Natural Science Foundation of China (Grant No. 42175070). Yimin LIU and Zhixiang LI were also supported by the National Natural Science Foundation of China (Grant No. 42288101). This study was supported by the National Key Scientific and Technological Infrastructure project “Earth System Numerical Simulation Facility” (EarthLab).

Data availability statement

The ERA5 data were downloaded from https://apps.ecmwf.int/data-catalogues/era5/?class=ea. The S2S database is available at https://apps.ecmwf.int/datasets/data/s2s/levtype=sfc/type=cf/.

Author contributions

ZL performed the analysis, developed the diagnostic method, drafted and revised the manuscript. JL conceptualized and supervised the study, drafted and revised the manuscript. YL revised the manuscript and supervised the study.

Conflict of Interest Disclosure

The authors declare there are no conflicts of interest for this manuscript.

https://doi.org/10.5194/egusphere-2026-1156
Preprint. Discussion started: 23 March 2026

References

Bordoni, S., and Schneider, T.: Monsoons as eddy-mediated regime transitions of the tropical overturning circulation, Nat. Geosci., 1, 515–519, https://doi.org/10.1038/ngeo248, 2008.

Breeden, M. L., Albers, J. R., Butler, A. H., and Newman, M.: The spring minimum in subseasonal 2-meter temperature forecast skill over North America, Mon. Weather Rev., 150, 2617–2628, https://doi.org/10.1175/MWR-D-22-0062.1, 2022.

Berthou, S., Renshaw, R., Smyth, T., et al.: Exceptional atmospheric conditions in June 2023 generated a northwest European marine heatwave which contributed to breaking land temperature records, Commun. Earth Environ., 5, 287, https://doi.org/10.1038/s43247-024-01413-8, 2024.

Cheung, H. N., Zhou, W., Mok, H. Y., et al.: Revisiting the climatology of atmospheric blocking in the Northern Hemisphere, Adv. Atmos. Sci., 30, 397–410, https://doi.org/10.1007/s00376-012-2006-y, 2013.

Fei, C., and White, R. H.: The role of topography, land and sea surface temperature on quasi-stationary waves in Northern Hemisphere winter: insights from CAM6 simulations, Weather Clim. Dynam., 6, 1119–1146, https://doi.org/10.5194/wcd-6-1119-2025, 2025.

Fragkoulidis, G., and Wirth, V.: Local Rossby wave packet amplitude, phase speed, and group velocity: Seasonal variability and their role in temperature extremes, J. Climate, 33, 8767–8787, https://doi.org/10.1175/JCLI-D-19-0377.1, 2020.

Gao, J., and Gao, H.: "Wheat-Soaked Persistent Precipitation" in Late Spring 2023 in the Huang-Huai-Hai Plain and the Large-Scale Circulation Pattern, Meteorol. Mon., 49, 1227–1234, https://doi.org/10.7519/j.issn.1000-0526.2023.082901, 2023. (in Chinese)

Hersbach, H., Bell, B., Berrisford, P., Hirahara, S., Horányi, A., Muñoz-Sabater, J., et al.: The ERA5 global reanalysis, Q. J. R. Meteorol. Soc., 146, 1999–2049, https://doi.org/10.1002/qj.3803, 2020.

Hoskins, B. J., and Ambrizzi, T.: Rossby wave propagation on a realistic longitudinally varying flow. J. Atmos. Sci., 50, 1661–1671, https://doi.org/10.1175/1520-0469(1993)050<1661:RWPOAR>2.0.CO;2, 1993.

Huang, B., Thorne, P. W., Banzon, V. F., Boyer, T., Chepurin, G., Lawrimore, J. H., Menne, M. J., Smith, T. M., Vose, R. S., and Zhang, H.-M.: Extended Reconstructed Sea Surface Temperature, Version 5 (ERSSTv5): Upgrades, Validations, and Intercomparisons, J. Climate, 30, 8179–8205, https://doi.org/10.1175/JCLI-D-16-0836.1, 2017.

Huffman, G. J., Adler, R. F., Morrissey, M. M., Bolvin, D. T., Curtis, S., Joyce, R., et al.: Global precipitation at one-degree daily resolution from multisatellite observations, J. Hydrometeorol., 2, 36–50, https://doi.org/10.1175/1525-7541(2001)002<0036:gpaodd>2.0.co;2, 2001.

Jain, P., Barber, Q. E., Taylor, S. W., Whitman, E., Castellanos-Acuna, D., Boulanger, Y., et al.: Drivers and Impacts of the Record-Breaking 2023 Wildfire Season in Canada, Nat. Commun., 15, 6764, https://doi.org/10.1038/s41467-024-51154-7, 2024.

Kautz, L.-A., Martius, O., Pfahl, S., Pinto, J. G., Ramos, A. M., Sousa, P. M., and Woollings, T.: Atmospheric blocking and weather extremes over the Euro-Atlantic sector – a review, Weather Clim. Dynam., 3, 305–336, https://doi.org/10.5194/wcd-3-305-2022, 2022.

Li, Z., Lu, J., and Liu, Y.: The Period and Phase Speed of Upper-tropospheric Planetary- and Synoptic-scale Waves during the Solstice Seasons: Climatology and Trends during 1979–2023, Adv. Atmos. Sci., 42, 2223–2234, https://doi.org/10.1007/s00376-024-4236-1, 2025.

https://doi.org/10.5194/egusphere-2026-1156
Preprint. Discussion started: 23 March 2026

Lubis, S. W., Chen, Z., Lu, J., Hagos, S., Chang, C.-C., and Leung, L. R.: Enhanced Pacific Northwest heat extremes and wildfire risks induced by the boreal summer intraseasonal oscillation. npj Clim. Atmos. Sci., 7, 232, https://doi.org/10.1038/s41612-024-00766-3, 2024.

Luo, D., Cha, J., Zhong, L., and Dai, A.: A nonlinear multiscale interaction model for atmospheric blocking: The eddy-blocking matching mechanism, Q. J. R. Meteorol. Soc., 140, 1785–1808, https://doi.org/10.1002/qj.2337, 2014.

Luo, D., Chen, X., Overland, J., Simmonds, I., Wu, Y., and Zhang, P.: Weakened Potential Vortility Barrier Linked to Recent Winter Arctic Sea Ice Loss and Midlatitude Cold Extremes, J. Climate, 32, 4235–4261, https://doi.org/10.1175/JCLI-D-18-0449.1, 2019.

Lupo, A. R.: Atmospheric blocking events: a review, Ann. N. Y. Acad. Sci., 1504, 5–24, https://doi.org/10.1111/nyas.14557, 2021.

Mu, M., and Duan, W.: A nonlinear theory and technology for reducing the uncertainty of high-impact ocean–atmosphere event prediction, Adv. Atmos. Sci., 42, 1981–1995, https://doi.org/10.1007/s00376-025-4467-9, 2025.

Nakamura, N., and Huang, C. S. Y.: Atmospheric blocking as a traffic jam in the jet stream, Science, 361, 42–47, https://doi.org/10.1126/science.aat0721, 2018.

Pelly, J. L., and Hoskins, B. J.: A new perspective on blocking, J. Atmos. Sci., 60, 743–755, https://doi.org/10.1175/1520-0469(2003)060<0743:ANPOB>2.0.CO;2, 2003.

Takaya, K., and Nakamura, H.: A formulation of a phase-independent wave activity flux for stationary and migratory quasigeostrophic eddies on a zonally varying basic flow, J. Atmos. Sci., 58, 608–627, https://doi.org/10.1175/1520-0469(2001)058<0608:AFOAPI>2.0.CO;2, 2001.

Tibaldi, S., and Molteni, F.: On the operational predictability of blocking, Tellus A, 42, 343–365, https://doi.org/10.3402/tellusa.v42i3.11882, 1990.

van Mourik, J., de Vries, H., and Baatsen, M.: On the movement of atmospheric blocking systems and the associated temperature responses, Weather Clim. Dynam., 6, 413–429, https://doi.org/10.5194/wcd-6-413-2025, 2025.

White, R. H., and Mareshet Admasu, L.: Temporally and zonally varying atmospheric waveguides – climatologies and connections to quasi-stationary waves, Weather Clim. Dynam., 6, 549–570, https://doi.org/10.5194/wcd-6-549-2025, 2025.

Wu, D., Zhang, J., Niu, X., Shi, R., Wang, X., Liu, J., Wen, H., Zhou, Y., Pu, W., Zhang, B., Zhang, D., and Wang, X.: Triggers of the record‐breaking 2023 Canadian wildfires: Extreme heat waves and droughts driven by abnormally high sea surface temperatures. J. Geophys. Res.-Atmos., 130, e2025JD044451, https://doi.org/10.1029/2025JD044451, 2025.

Woollings, T., Barriopedro, D., Methven, J., et al.: Blocking and its response to climate change, Curr. Clim. Change Rep., 4, 287–300, https://doi.org/10.1007/s40641-018-0108-z, 2018.

Yao, W., Lu, J., and Liu, Y.: Rotational flow dominates abrupt seasonal change in zonally asymmetric tropical meridional circulation. Geophys. Res. Lett., 53, e2025GL118924, https://doi.org/10.1029/2025GL118924, 2026.

Yeh, T.-C., Dao, S.-Y., and Li, M.-T.: The abrupt change of circulation over the Northern Hemisphere during June and October, in: The Atmosphere and the Sea in Motion. The Rossby Memorial Volume, Bolin, B. (Ed.), Rockefeller Institute Press, New York, 249–267, 1959.

Yeh, T.-C., Tao, S.-Y., Chu, P.-C., and Chen, L. S.: Studies on the Blocking Situations in Northern Hemisphere Winter, Science Press, Beijing, China, 135 pp., 1962. (In Chinese)

https://doi.org/10.5194/egusphere-2026-1156
Preprint. Discussion started: 23 March 2026

Zhang, W., Wang, L., Luo, D., Yao, Y., Luo, B., Simmonds, I., and Semenov, V.: Impacts of background conditions on the evolutionary disparities between Greenland and Euro-Atlantic blocking. J. Atmos. Sci., 82(3): 501–517, https://doi.org/10.1175/JAS-D-24-0016.1, 2025.